Nuclear Materials and Energy 21 (2019) 100709

Contents lists available at ScienceDirect

Nuclear Materials and Energy

journal homepage: www.elsevier.com/locate/nme

Finite element analysis of hydrogen retention in ITER plasma facing components using FESTIM

Rémi Delaporte-Mathurin[*,a], Etienne A. Hodille[b], Jonathan Mougenot[c], Yann Charles[c], Christian Grisolia[a]

[a] CEA, IRFM, 13018 Saint-Paul-lez-Durance, France
[b] Department of Physics, University of Helsinki, PO Box 43, FI-00014, Finland
[c] Université Paris 13, LSPM, CNRS, Paris Sorbonne Cité, 99 avenue Jean-Baptiste Clément, F-93430 Villetaneuse, France

ARTICLE INFO

Keywords:
Fusion
Tritium
Finite elements
Plasma facing components
Hydrogen isotopes

ABSTRACT

The behaviour of hydrogen isotopes in ITER monoblocks was studied using the code FESTIM (Finite Element Simulation of Tritium In Materials) which is introduced in this publication. FESTIM has been validated by reproducing experimental data and the Method of Manufactured Solutions was used for analytical verification. Following relevant plasma scenarios, both transient heat transfer and hydrogen isotopes (HIs) diffusion have been simulated in order to assess HIs retention in monoblocks. Relevant materials properties have been used. Each plasma cycle is composed of a current ramp up, a current plateau, a current ramp down and a resting phase before the following shot. 100 cycles are simulated. The total HIs inventory in the tokamak during resting phases reaches 1.8×10^{-3} mg whereas during the implantation phases it keeps increasing as a power law of time. Particle flux on the cooling channel of the monoblock is also computed. The breakthrough time is estimated to be $t = 1 \times 10^{5}$ s which corresponds to 24 cycles. Relevance of 2D modelling has been demonstrated by comparing the total HIs inventory obtained by 2D and 1D simulations. Using 1D simulations, a relative error is observed compared to 2D simulations which can reach -25% during the resting phase. The error during implantation phases keeps increasing.

1. Introduction

In fusion reactors, plasma facing components (PFCs) are exposed to intense particle flux of hydrogen isotopes (HIs) as well as very high heat flux. These fluxes can respectively reach and 10 MW·m^{-2} in the divertor region. The material chosen to sustain such high fluxes is tungsten (W) in ITER. Fuel particles from the plasma can be implanted in the PFC and then diffuse into the material. HIs particles can then get trapped. This leads to several major issues.

First, the total tritium inventory must stay below the ITER safety limit of 700 g in PFCs [1,2]. Secondly, HIs can eventually reach the cooling pipes and contaminate the coolant. The amount of particles reaching the coolant must then be predicted. Finally, local accumulation of HIs particles and He produced by decay (as well as He plasma implantation and impurities transmutation by neutron bombardment) can lead to a modification of the material thermal properties such as its thermal conductivity [3–6]. PFCs could then be unable to exhaust heat from the plasma and could even be damaged by local melting.

In the present work, a code named "Finite Element Simulation of Tritium In Materials" (FESTIM) based on Macroscopic Rate Equations (MRE) has been developed. This tool is built upon the previous work made on MHIMS by Hodille *et al.* [7]. As in previous studies [8,9], this new code relies on FEniCS [10] and Finite Element Methods. FESTIM is able to simulate the diffusion and trapping of HIs as well as heat transfer in 1/2/3D multi-material domains, which allows to simulate laboratories experiments as well as PFCs in realistic tokamak environment. Section 2 describes the physical model chosen for the tool. We will then detail in Section 3 both the experimental validation and analytical verification of the code. Finally a simulation of a W monoblock under both heat and particle fluxes is presented and results are discussed in Section 4.

2. Model description

The model used in FESTIM is based on MRE models which have been widely used in previous studies [7,11]. As it has already been detailed in [7,12], only a general description will be made in this paper.

As in most of MRE models, HIs are split in several populations which

* Corresponding author.
E-mail address: remi.delaporte-mathurin@cea.fr (R. Delaporte-Mathurin).

https://doi.org/10.1016/j.nme.2019.100709
Received 24 July 2019; Received in revised form 16 September 2019; Accepted 27 September 2019
Available online 09 October 2019

are the mobile and the trapped ones on the i-th trap, described using their concentration (respectively c_m and $c_{t,i}$). The spatio temporal evolution of these concentrations are commonly described by the following reaction-diffusion system:

$$\frac{\partial c_m}{\partial t} = \nabla\cdot(D(T)\nabla c_m) - \sum \frac{\partial c_{t,i}}{dt} + S_{ext} \tag{1}$$

$$\frac{\partial c_{t,i}}{\partial t} = \nu_m(T)\cdot c_m\cdot(n_i - c_{t,i}) - \nu_i(T)\cdot c_{t,i} \tag{2}$$

In Eq. 1 the first term on the right hand side is derived from Fick's law, where $D(T) = D_0\cdot\exp\left(\frac{-E_{\text{diff}}}{k_B\cdot T}\right)$ is the diffusion coefficient of HIs in the considered material in $\text{m}^2\cdot\text{s}^{-1}$, T the temperature in K and $k_B = 8.6\times10^{-5}\text{eV}\cdot\text{K}^{-1}$ the Boltzmann constant. S_{ext} corresponds to an external source term corresponding to the HI implantation in PFCs expressed in $\text{m}^{-3}\cdot\text{s}^{-1}$ and $\sum\frac{\partial c_{t,i}}{dt}$ corresponds to the trapping and detrapping processes. In Eq. 2, the first term on the right hand side corresponds to the trapping of mobile particles. This process depends on the number of empty trapping sites $n_i - c_{t,i}$, the amount of mobile particles c_m and the rate $\nu_m = \frac{D(T)}{\lambda^2\cdot n_{\text{solute}}}$ in $\text{m}^3\cdot\text{s}^{-1}$ where λ is the lattice constant in m and n_{solute} is the density of interstitial sites in m^{-3}. The second term describes the detrapping process characterised by the rate $\nu_i = \nu_0\cdot\exp\left(\frac{-E_i}{k_B\cdot T}\right)$ expressed in s^{-1} where ν_0 is a pre-exponential factor, E_i is the detrapping energy of trap i. The unit of the different concentration, c_m, $c_{t,i}$ and n_{solute} are in m^{-3} but they can be expressed in atomic fraction (at.fr.) by normalising them to the atomic density of the material ρ (m^{-3}).

The heat equation is described as follow:

$$\mu\cdot C_p\frac{\partial T}{\partial t} = \nabla\cdot(\lambda\nabla T) \tag{3}$$

where μ is the density of the material in $\text{kg}\cdot\text{m}^{-3}$, C_p its specific heat capacity expressed in $\text{J}\cdot\text{kg}^{-1}\cdot\text{K}^{-1}$ and λ the thermal conductivity expressed in $\text{W}\cdot\text{K}^{-1}$.

Eqs. 1 and 2 (and if needed Eq. 3) are then solved using FESTIM.

3. FESTIM validation and verification

To demonstrate FESTIM's robustness and reliability, a thorough verification and validation process has been carried out including analytical verification and comparison against experiments.

3.1. Analytical verification against a known solution

Although validation against experiments could show that FESTIM is able reproduce the data with a given set of parameters, objective verification against analytical solutions is first required to ensure that the governing Eqs. 1 and 2 are solved correctly.

For this verification case, a 1D slab is considered with a thickness l. The concentration of mobile particles was set to c_0 on one side of the slab and set to zero on the other side. Only one trap is considered in this case and its density n_1 is homogeneously distributed.

The trapping parameter ζ is defined in [13] as follow:

$$\zeta = \frac{\lambda^2\, n_{\text{solute}}\,\nu_0}{D_0\, n_1}\exp\left(\frac{E_{\text{diff}} - E_1}{k_B\, T}\right) + \frac{c_m}{n_1} \tag{4}$$

In our case, we choose the detrapping energy E_1, the concentration c_0 and the temperature T so that $\zeta \gg \frac{c_m}{n_1}$. This is known as the *effective diffusivity regime* where the diffusion is almost identical to the case where there are no traps. The coefficient D is then replaced by an effective diffusion coefficient:

Table 1
Parameters used for the analytical verification .

Parameter	Units	Value
ρ	m^{-3}	3.16×10^{22}
n_1		$1.00\times10^{-1}\rho$
c_0		$1.00\times10^{-4}\rho$
n_{solute}		2ρ
E_1	eV	8.6×10^{-3}
E_{diff}		0
λ	m	3.16×10^{-8}
l		5×10^{-5}
T	K	1000
t_f	s	10^{-8}
ν_0	s^{-1}	10^{13}
D_0	$\text{m}^2\cdot\text{s}^{-1}$	1

$$D_{\text{eff}} = \frac{D}{1 + \frac{1}{\zeta}} \tag{5}$$

The particle flux at the background surface is expressed in $\text{H}\cdot\text{m}^{-2}\cdot\text{s}^{-1}$ and finally defined in [13] by:

$$\varphi_H(t) = \frac{c_0 D}{l}\left[1 + 2\sum_{m=1}^{\infty}(-1)^m\exp\left(-m^2\frac{\pi^2\, D_{\text{eff}}\, t}{l^2}\right)\right] \tag{6}$$

All the parameters are defined in Table 1. These parameters have been chosen for the sake of verification and do not necessarily represent realistic conditions as verification is a mathematical exercise.

One can notice on Figure 1 that the numerical results are in good agreement with the analytical solution.

The maximum error between analytical and numerical solutions is calculated to be $6.56\times10^{20}\,\text{H}\cdot\text{m}^{-2}\cdot\text{s}^{-1}$ with 50,000 piecewise linear elements (P1) which corresponds to 1% of the maximum value. According to finite elements theory, this value will decrease with the stepsize and with the element size.

3.2. Analytical verification using MMS

To unravel the complexity of governing equations, the Method of Manufactured Solutions (MMS) is often used [14,15]. Manufactured solutions are exact solutions that have been modified with additional source terms. The sets of source terms and boundary conditions obtained are then fed into FESTIM and the error is measured.

At this extent the following manufactured solutions are chosen:

$$\begin{cases} c_{m_D} = 1 + x^2 + n(t) \\ c_{t,1_D} = 1 + x^2 + \cos(t) \end{cases} \tag{7}$$

By combining Eqs. 1, 2 and 7, one can obtain the following source terms:

$$\begin{cases} f = \cos(t) - n(t) - 2D \\ g_1 = \nu_1 c_{t,1_D} - \nu_m c_{m_D}(n_1 - c_{t,1_D}) - n(t) \end{cases} \tag{8}$$

where g_1 is an additional source term in Eq. 2. The Dirichlet boundary conditions for c_m and $c_{t,1}$ are:

$$\begin{cases} c_m = 1 + x^2 + n(t) \quad \text{on } \partial\Omega \\ c_{t,1} = 1 + x^2 + \cos(t) \quad \text{on } \partial\Omega \end{cases} \tag{9}$$

where $\partial\Omega$ is the boundary of the domain. Finally, initial values for c_m and $c_{t,i}$ are:

$$\begin{cases} c_m(t=0) = 1 + x^2 \\ c_{t,1}(t=0) = 2 + x^2 \end{cases} \tag{10}$$

Once all these parameters are fed into FESTIM, one can easily compare the computed solution with the exact solution in Eq. 7. The L2-norm E_{c_m}

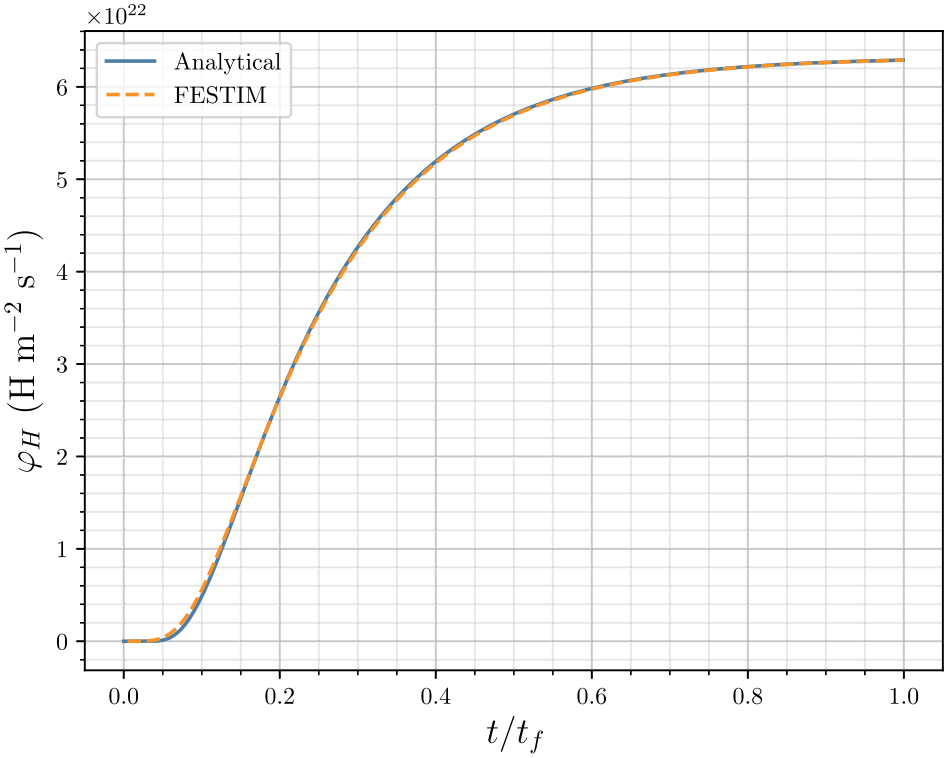

Fig. 1. Temporal evolution of the particle flux φ_H ($t_f = 10^{-8}$s).

can then be calculated as follow:

$$E_{c_m} = \sqrt{\int_\Omega (c_{m_D} - c_m)^2 dx} \tag{11}$$

The evolution of E_{c_m} as function of the element size h is shown on Fig. 2. One can notice that E_{c_m} increases as $A \cdot h^k$. This is known as the *asymptotic regime* and the coefficient k is called the convergence rate. k typically tends to N + 1 as h approaches 0, N being the order of the finite elements. In this simulation, k approaches 2 as expected since elements of order 1 have been used.

The results of the verification cases studied in Sections 3.1 and 3.2 show that FESTIM reliably solves the governing Eqs. 1 and 2. It has also been shown that the convergence rate is in accordance with the theory of finite elements meaning that the code is free of errors that could lead to unreliable results in the future. Validation can then be performed to ensure that the MRE model described in Section 2 can be used to reproduce experimental results.

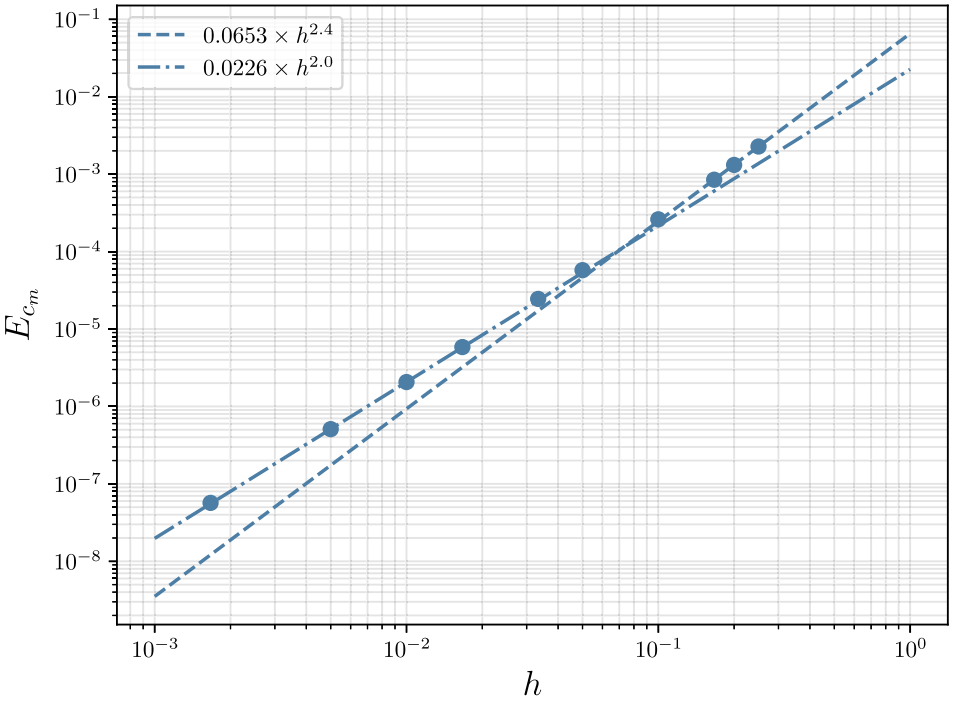

Fig. 2. Evolution of the L2 norm of the error as function of element size h.

3.3. Validation against experimental data

In order to further validate the model, the laboratory experiments from Ogorodnikova *et al* [16] are simulated. We choose these particular experiments as it has already been simulated several times in [7,11,16,17]. Therefore, this simulation can be used as a benchmark case for FESTIM.

In this experiment, after deuterium (D) implantation in hot-rolled tungsten (W), Temperature Programmed Desorption (TPD) is performed. TPD consists in heating the sample with a well controlled temperature ramp and measure with a mass spectrometer the evolution of the amount of desorbed particles with respect to temperature. This results in a TPD spectrum. In order to reproduce this spectrum, three phases are simulated.

The first one is the implantation phase where the source term in Eq. 1 is $S_{ext} = (1 - r)\cdot\varphi\cdot f(x)$, r being the reflection coefficient (*i.e.* the proportion of particles which are reflected from the surface to the plasma), φ the incident ion flux in $m^{-2}\cdot s^{-1}$ and $f(x)$ a Gaussian distribution with R_p its mean value and *gma* its width. The parameters of $f(x)$ are determined with the software SRIM [18]. This phase lasts t_{imp} and the temperature is $T = T_{imp}$.

The second phase is the resting period where the source is turned off (*i.e.* $S_{ext} = 0$) for a time t_{rest} at $T = T_{rest}$.

Finally, the last period is the TPD where temperature is increased linearly with a given heating ramp β.

In order to fit the experimental results, three traps are needed: two intrinsic traps and one extrinsic trap to account for the creation of ion-induced defects during the implantation. Extrinsic traps can be created by either supersaturation of HIs in the implantation range $f(x)$ creating monovacancies [19–23], that can lead to vacancy clusters and bubbles [16,24] or local stress field [25,26]. According to [23], mono-vacancies can be created in the implantation zone when W is exposed to D ion flux if the flux is higher than a threshold limit for a given temperature. At the temperature of the considered experiment (300 K), the threshold flux is $10^{18}\,m^{-2}\cdot s^{-1}$ which is lower than the flux in the experiment (see Table 2).

The evolution of the extrinsic trap density is given by Eq. 12.

Table 2
Parameters used for experimental validation.

Parameter	Units	Value
ρ_W	m^{-3}	6.3×10^{28}
n_{solute}		$6\,\rho_W$
n_1		$1 \times 10^{-3}\rho_W$
n_2		$4 \times 10^{-4}\rho_W$
$n_{3a_{max}}$		$1 \times 10^{-1}\rho_W$
$n_{3b_{max}}$		$1 \times 10^{-2}\rho_W$
E_{diff}	eV	0.39
E_1		0.87
E_2		1.00
E_3		1.50
η_a	-	6×10^{-4}
η_b	-	2×10^{-4}
λ	m	110×10^{-9}
x_p		1×10^{-6}
R_p		4.5×10^{-9}
gma		4.5×10^{-9}
T_{imp}	K	300
T_{rest}		300
t_{imp}	s	400
t_{rest}		50
ν_0	s^{-1}	10^{13}
β	$K\cdot s^{-1}$	8
D_0	$m^2\cdot s^{-1}$	4.1×10^{-7}
φ	$m^{-2}\cdot s^{-1}$	2.5×10^{19}
r	-	0

$$\frac{dn_3}{dt} = (1 - r)\,\varphi\,\Big[\left(1 - \frac{n_3}{n_{3a_{max}}}\right)\eta_a f(x) + \left(1 - \frac{n_3}{n_{3b_{max}}}\right)\eta_b\,\theta_{xp}(x)\Big] \tag{12}$$

where $\theta_{xp}(x) = \frac{1}{x_p} \quad \forall\, x < x_p$, η_a and η_b are the rates of traps creation and $n_{3a_{max}}$ and $n_{3b_{max}}$ are their maximum values. This formulation follows the one proposed in [7,17] based on the expression of Ogorodnikova *et al.* [16].

All the above parameters are presented in Table 2. These parameters are in good agreement with those used in [7,11,17].

The simulated TPD spectrum is represented on Fig. 3.

One can see that the spectra produced by FESTIM and by Ogorodnikova *et al.* [16] are in good agreement. One peak can be distinguished at 450 K with two pronounced shoulders at 500 K and 620 K. As denoted by the arrow in Fig. 3, the peak at 450 K corresponds to the detrapping from the low-energy high-concentration trap and the shoulders at 500 K and 620 K correspond to detrapping from 1.00 eV and 1.50 eV trap, respectively.

It has therefore been verified that FESTIM solves its governing equations correctly and that it can be reliably used in order to reproduce laboratory experiments.

4. Monoblock simulation

4.1. Problem description

Because of its high melting point, low solubility for hydrogen and low sputtering yield, W is the chosen material for the divertor. Thorough studies have been performed on W and its properties are well known. For the coolant tube of the divertor, copper (Cu) and Cu alloys are leading candidates as they feature very high thermal conductivity. In this paper, W monoblocks with CuCrZr cooling pipes and Cu interlayers are simulated, according to Fig. 4. In our case, the dimensions of the monoblock are $H = 29$ mm, $L = 15$ mm, $D_1 = 12$ mm, $D_2 = 15$ mm and $D_3 = 16$ mm. The monoblock's thickness is $l = 12$ mm.

The materials properties are presented in Table 3.

In accordance with [1], two intrinsic traps are used in the W whereas only one is set in the CuCrZr. These traps are homogeneously distributed. Ion-induced traps in the first μm are not taken into account as their impact on the macroscopic behaviour is assumed to be quite low. Traps parameters are described in Table 4. The rest of the parameters are defined in Section 3.3.

The upper surface of the monoblock (red on Fig. 4) is exposed to the plasma and therefore to a heat flux φ_T and a particle flux φ_H.

A Robin condition is applied on the upper surface and takes into account the implantation of incident ions and the recombination of HIs ions to HIs molecules at the surface. This condition is defined as:

$$-D(T)\overrightarrow{\nabla c_m}\cdot\overrightarrow{n} = (1 - r)\varphi_H - K_{r_W}(T)\,c_m^2 \tag{13}$$

where $\overrightarrow{n}$ is the normal vector. Only a part of the incident flux is implanted. The remaining part is reflected. The reflection coefficient r is equal to the ratio of the reflected particles over the implanted ones. The recombination coefficient K_{r_W} is defined as:

$$K_{r_W}(T) = 3.2 \times 10^{-15}\exp\left(\frac{-1.16}{k_B\,T}\right) \tag{14}$$

The above Anderl's recombination coefficient [29] has been used in several studies [30,31] and is expressed in $H^{-1}\cdot m^{-2}\cdot s^{-1}$. To reproduce realistic tokamak scenario, 100 plasma cycles are simulated. Each cycle is made of four phases as shown on Fig. 5. The first one is a current and density ramp up phase which lasts 100 *s* and during which the sources from the plasma are linearly increasing. Then there is a 400 *s* plateau phase during which φ_H and φ_T are constant. The next phase is a current and density ramp down where the sources are gradually switched off

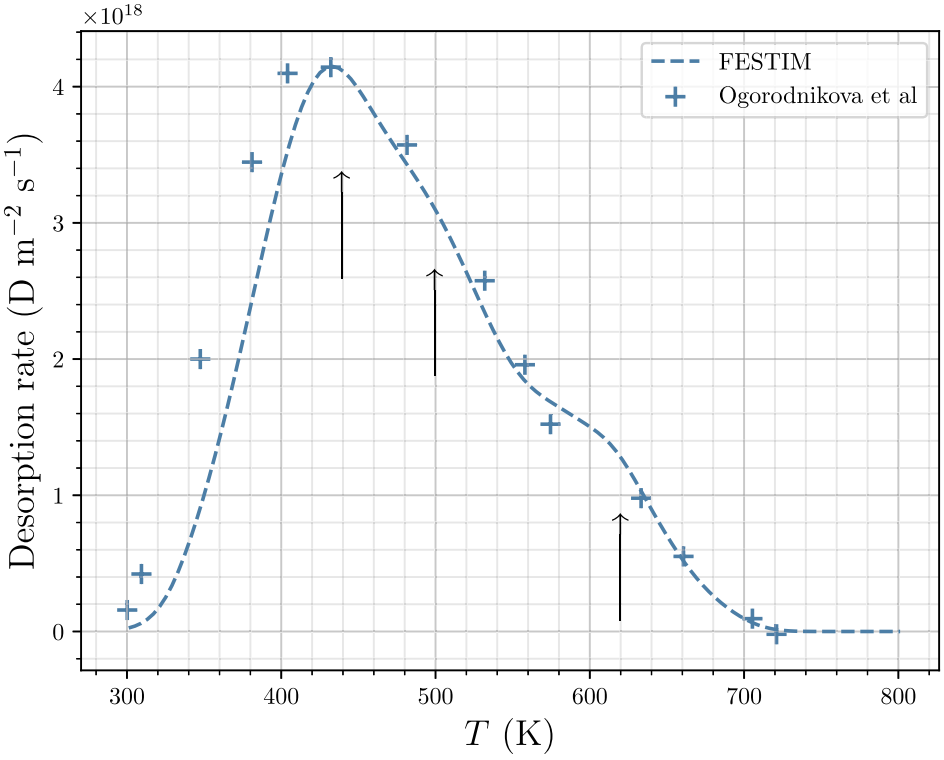

Fig. 3. TPD spectrum simulated by FESTIM compared to experimental data of Ogorodnikova *et al.* [16]. Arrows correspond to the three desorption peaks.

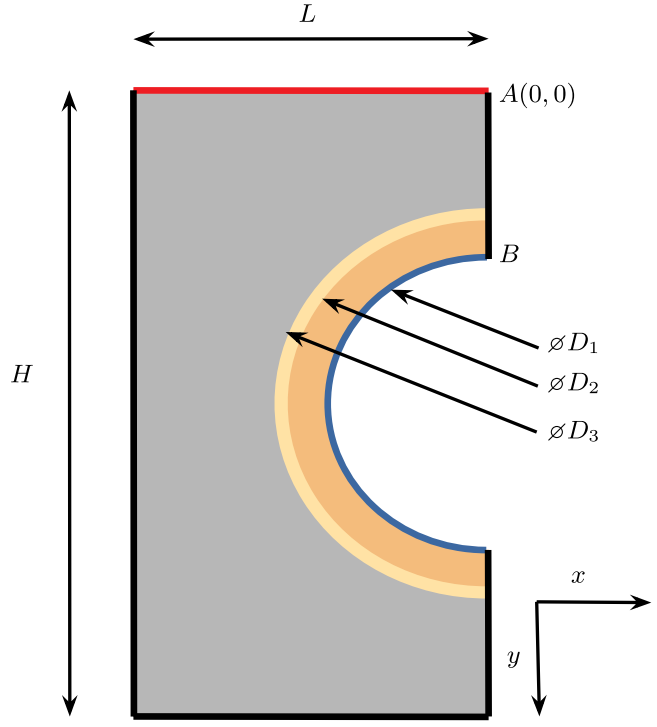

Fig. 4. Diagram of a monoblock showing W, Cu, CuCrZr alloy, surface exposed to plasma and cooling surface.

followed by a resting phase of 1h. Each cycle thus lasts 4200 *s*.

On the cooling surface (blue on Fig. 4), a convective flux condition is set with a heat transfer coefficient $h = 70,000\ \mathrm{W{\cdot}m^{-2}{\cdot}K^{-1}}$ and a coolant temperature $T_{coolant} = 323.15\,\mathrm{K}$. These parameters are of the same order of magnitude as the one used in [32]. The following recombination flux is also applied on the cooling surface:

$$-D(T)\overrightarrow{\nabla c_m}\cdot\overrightarrow{n} = -K_{r_{\mathrm{CuCrZr}}}(T)\,c_m^2 \tag{15}$$

where:

$$K_{r_{\mathrm{CuCrZr}}}(T) = 2.9\times10^{-14}\exp\left(\frac{-1.92}{k_B\,T}\right) \tag{16}$$

The above recombination coefficient expressed in $\mathrm{H^{-1}{\cdot}m^{-2}{\cdot}s^{-1}}$ was found in [33]. These conditions are constant throughout the plasma cycle. Solute concentration continuity is assumed at interfaces between Cu and CuCrZr and between Cu and W.

Every other surfaces (black in Fig. 4) are assumed to be insulated in both thermal and HIs diffusion problems.

2D transient simulations on a 75,366-element unstructured mesh have been performed with FESTIM in order to assess HIs diffusion and retention in monoblocks. Piece-wise linear elements have been used.

4.2. Results

4.2.1. Temperature field

Due to the very high conductivity of the materials leading to a Biot number $Bi \gg 1$ and a small thermal time constant $\tau = \frac{2\rho C_p HL}{\pi h D_1} \approx 1\,\mathrm{s}$, the monoblock responds quickly to the different phases and the temperature field is identical from one cycle to another. Temperature field during the plateau is shown on Fig. 6.

One can observe the maximum temperature reached on the top surface of the monoblock is 1239 K. The maximum temperature reached in Cu and CuCrZr are respectively 636 K and 613 K. The temperature field is consistent with the one obtained in [32]. The temperature profile along the segment AB is shown on Fig. 7 and the temperature profiles along the x axis are shown on Fig. 8.

4.2.2. Evolution of the retention

Retention fields are represented on Fig. 9 during the several resting phases.

For visualisation purposes, the colour map has been modified. The maximum value is then higher than $1.0\times10^{21}\,\mathrm{m^{-3}}$ as shown on Fig. 10.

Table 3
Materials properties used in the simulations [27,28].

Material	C_p(J·kg^{-1}·K^{-1})	λ(W·K^{-1})	μ(kg·m^{-3})	D_0(m^2·s^{-1})	E_{diff} (eV)	α(×10^{-10}m)	β(×10^{29}m^{-3})
W	137	150	19,300	4.1×10^{-7}	0.39	1.1	3.7
CuCrZr	400	300	8960	6.6×10^{-7}	1.00	1.1	3.7
Cu	380	350	8900	3.5×10^{-5}	0.67	1.1	3.7

Table 4
Traps properties used in the simulations [1,7,28] .

	Material	$E_{t,i}$ (eV)	n_i(m^{-3})
Trap 1	W	0.87	$1.3 \times 10^{-3}\rho_W$
Trap 2	W	1.00	$3.5 \times 10^{-4}\rho_W$
Trap 3	CuCrZr	0.50	3.7×10^{24}

One can observe on Fig. 9a that the retention field at $t = 5012$ s (*i.e.* 2nd cycle) is already no longer 1D as the isovalues are not horizontal. Edge effects have become non negligible.

Retention on the symmetry axis (*i.e.* segment AB on Fig. 4) is plotted on Fig. 10. One can see the migration front goes deeper into the bulk after several cycles and eventually reaches the Cu inter-layer and then the cooling channel. The high retention zone near the W/Cu interface is due to the relatively low local temperature and the relatively high trap density compared to Cu.

The total HIs inventory in the monoblock is then obtained by integrating the retention field over the 2D domain and multiplying it by its thickness $l = 12$ mm and its temporal evolution is presented on Fig. 11.

It is shown that retention seems to be globally increasing. Over each cycle, one can see two strong variations when fluxes are increased and decreased. These are caused by the variation of the heat flux and the particle flux during the ramp up and ramp down phases. As temperature increases during the ramp up phase, traps in the near surface empty and a part of the HIs particle desorb from the surface. During the plateau phase, retention slowly increases as expected. When the sources are then switched off, the temperature progressively decreases and reaches

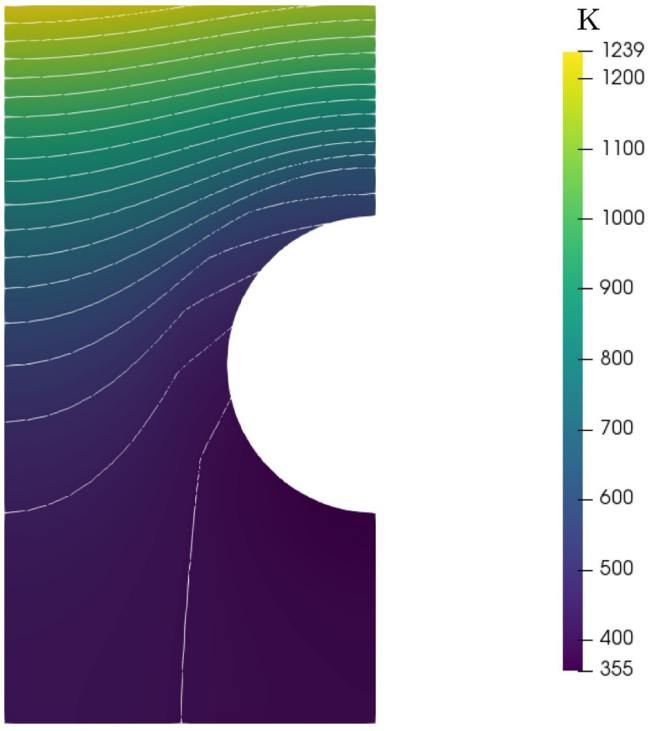

Fig. 6. Temperature field during the plateau phase.

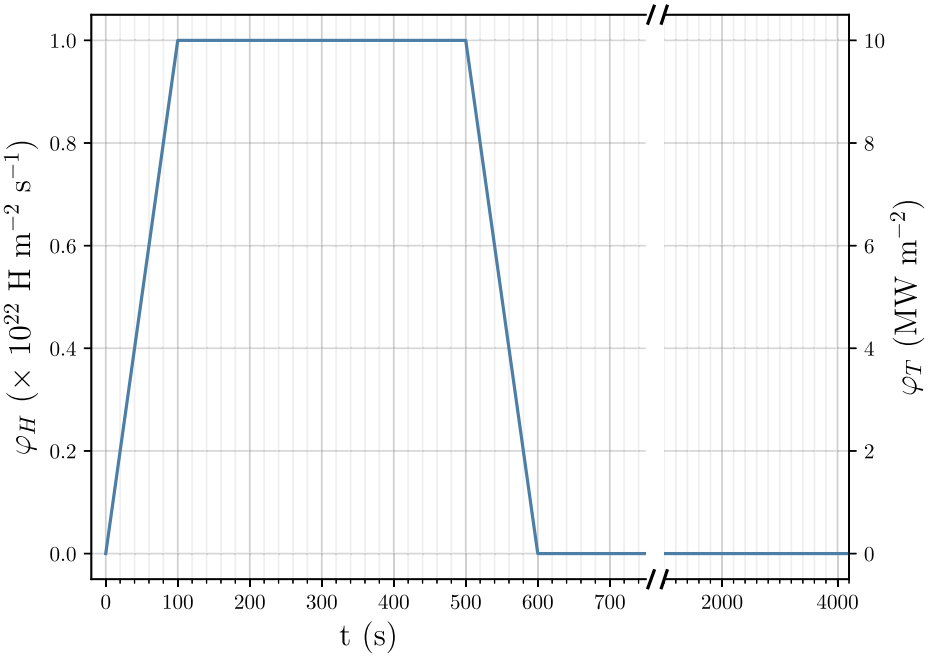

Fig. 5. Evolution of φ_T and φ_H during one plasma cycle.

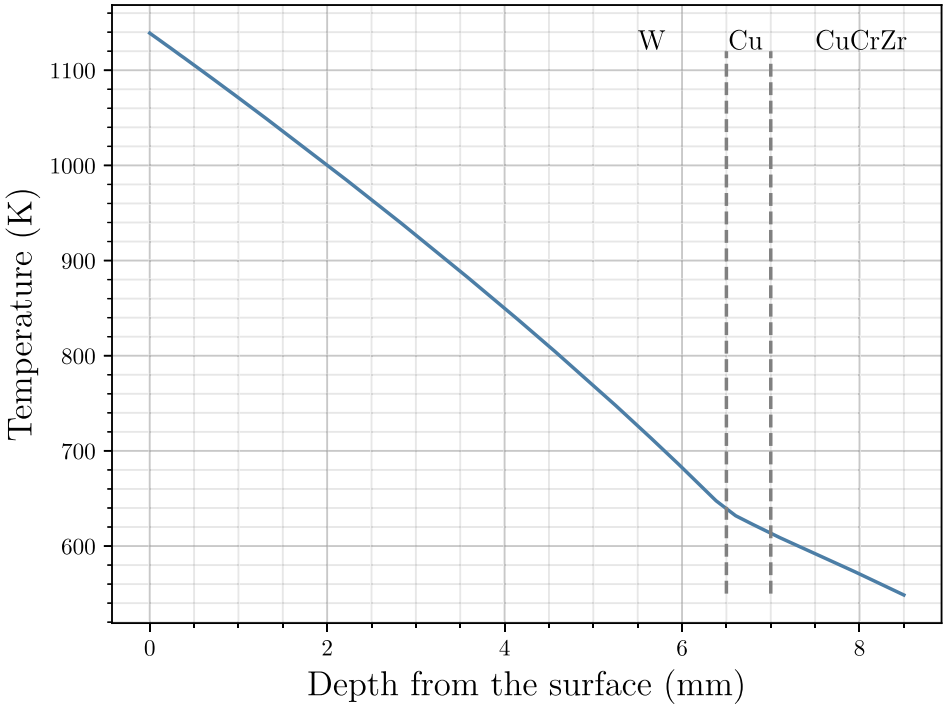

Fig. 7. Temperature profile along the segment AB during the plateau phase.

$T_{coolant}$. At the same time, the incident flux of particles also decreases maintaining the concentration of mobile particles relatively high in the material. Eventually, the temperature is low enough and the amount of particle implanted is high enough so that trapping become predominant over detrapping [34]. Since the ramp down only lasts a limited amount of time, HIs concentration increases significantly only at the near surface, as shown on Fig. 10. It can also be shown that the retention value deeper in the bulk does not increase as much as in the near surface. The increase of retention is therefore mostly caused by the variations in the first mm. Once the fluxes have reached zero, the temperature in the whole monoblock reaches $T_{coolant}$. The low concentration of mobile particles on the surface and the low temperature lead to very few desorption on the top surface and on the cooling surface. Retention during the resting phase is therefore nearly constant. As soon as the wall is heated at the beginning of the next cycle, temperature on the surface increases leading to surface desorption. On the other hand, retention during the implantation phases increases from one cycle to another and follows a power law.

The HIs inventory of the whole tokamak can then be obtained (assuming a similar behaviour for every monoblocks) by multiplying by

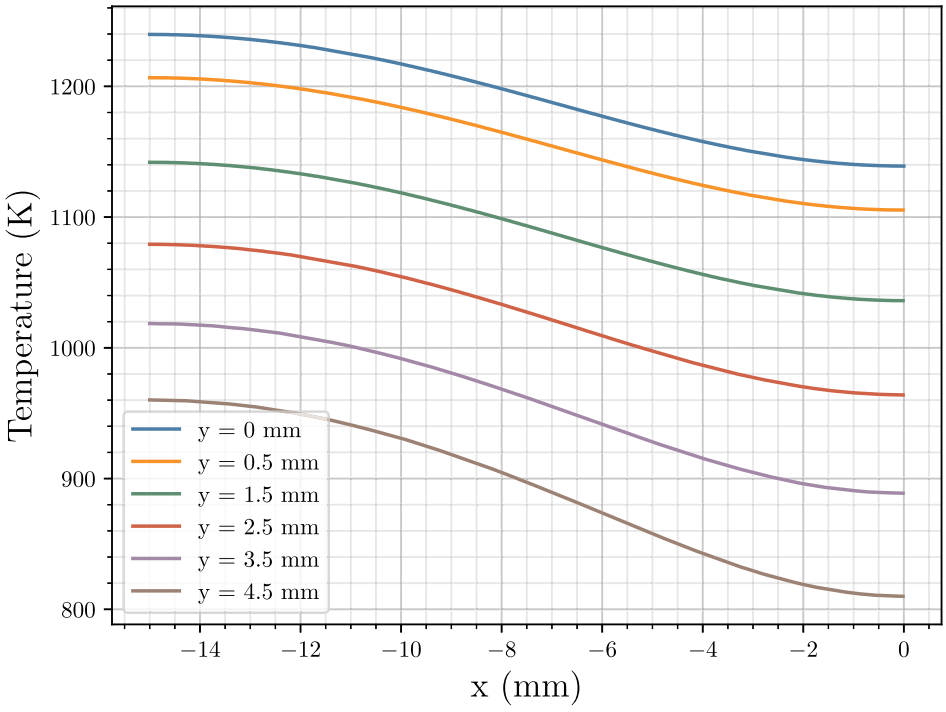

Fig. 8. Horizontal temperature profiles in the monoblock during the plateau phase.

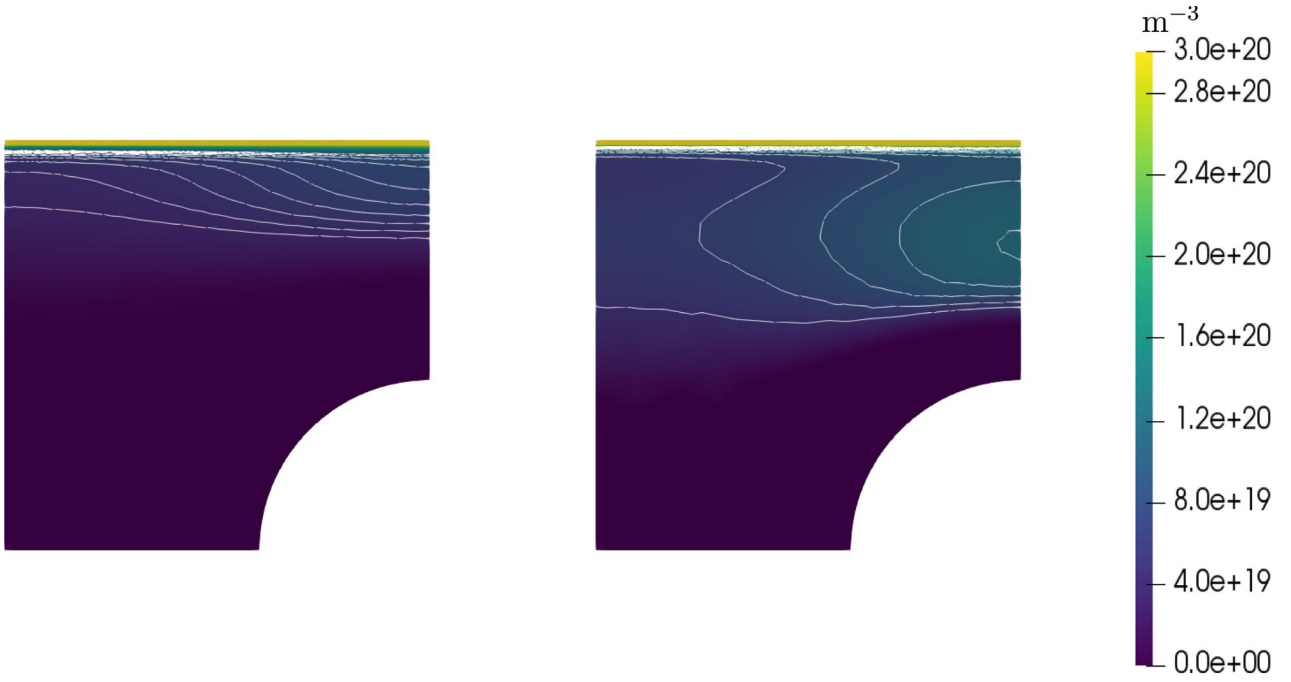

(a) $t = 5012\,\mathrm{s}$ (2nd cycle) (b) $t = 38{,}602\,\mathrm{s}$ (10th cycle)

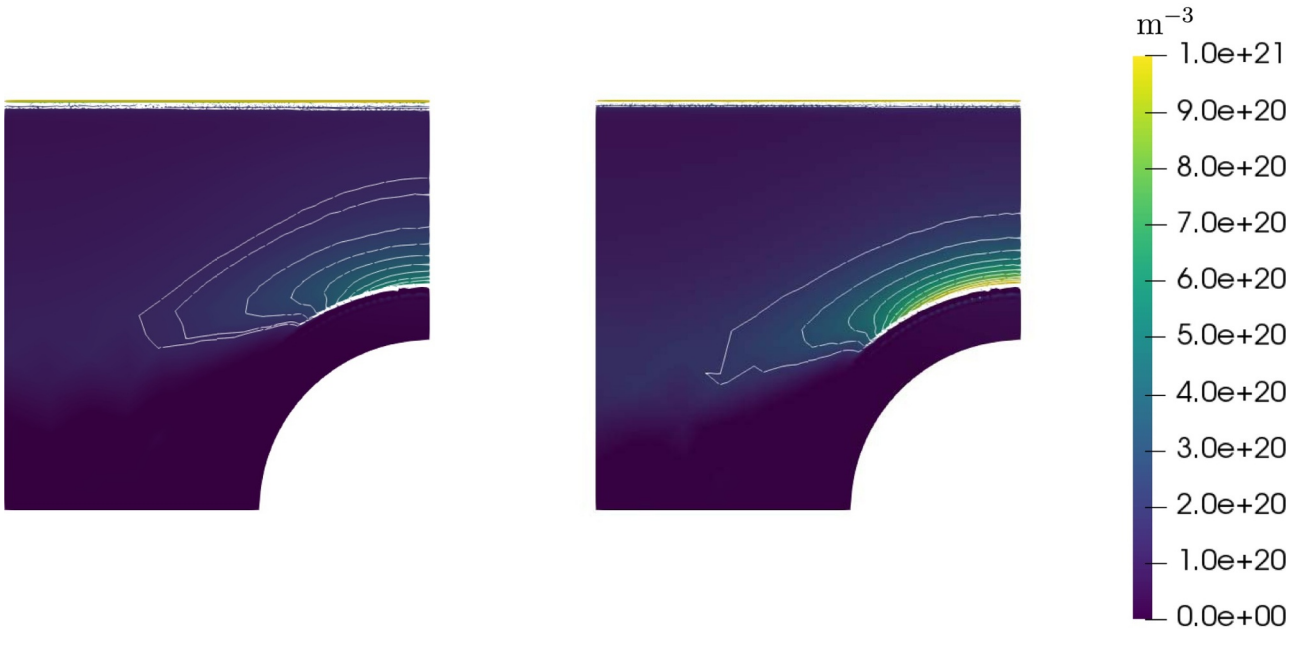

(c) $t = 210{,}803\,\mathrm{s}$ (50th cycle) (d) $t = 420{,}802\,\mathrm{s}$ (100th cycle)

Fig. 9. Retention fields.

the total number of plasma wet monoblocks in the divertor. Considering a surface of 10 m^2, the number of monoblocks is 27,777. The total amount of HIs retained in the tokamak after 100 plasma cycles would then be 1.8 mg which represents 2.5×10^{-4}% of the previously mentioned ITER safety limit. It is important to note that this estimation is a lower limit as the temperature reached in this simulation will only be encountered in the strike point region and not in all monoblocks. As shown in [1], where the same trapping parameters were used, the retention is maximum where the temperature is much lower (around 450 K).

4.2.3. Flux in coolant

Flux on the cooling surface (blue on Fig. 4) is computed with FESTIM by integrating on the cooling channel and multiplying it by the thickness l of the monoblock. It is shown on Fig. 12.

By using the steepest tangent one can estimate the breakthrough time at approximately $t = 1e5s$ which corresponds to 24 cycles. Firstly the flux derivative increases and then reaches an inflexion point. After $t = 16 \times 10^4\,\mathrm{s}$, the derivative decreases and the flux value seems to reach a maximum below $1.2 \times 10^{-11}\mathrm{g{\cdot}s^{-1}}$. This could imply a pseudo-steady state solution for the total inventory. Again by extrapolating to the whole divertor, the total flux for 27,777 monoblocks could reach

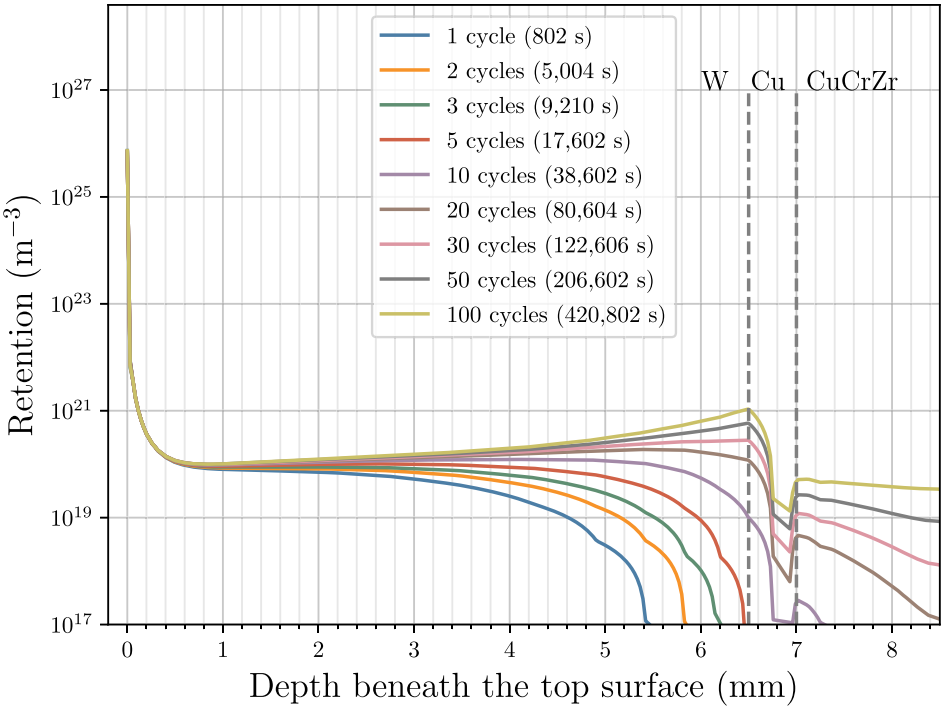

Fig. 10. Retention profiles along segment AB after several plasma cycles during resting phases.

3.19×10^{-7} g·s^{-1}.

4.2.4. Comparison with 1D simulations

To investigate the relevance of 2D modelling, 1D simulations have been performed. The uni-dimensional domain AB on Fig. 4 is considered and the same boundary conditions are set. By integrating the retention profile and multiplying it by the dimensions l and L, the resulting inventory is represented on Fig. 11. The relative error between 1D and 2D simulations is shown on Fig. 13 and calculated as follow:

$$\Delta_{\text{inv}} = \frac{\text{inv}_{1D} - \text{inv}_{2D}}{\text{inv}_{2D}} \tag{17}$$

where

$$\text{inv}_{1D} = lL \int_{AB} (c_{m,1D} + \sum c_{t,i,1D})\, dx \tag{18}$$

and

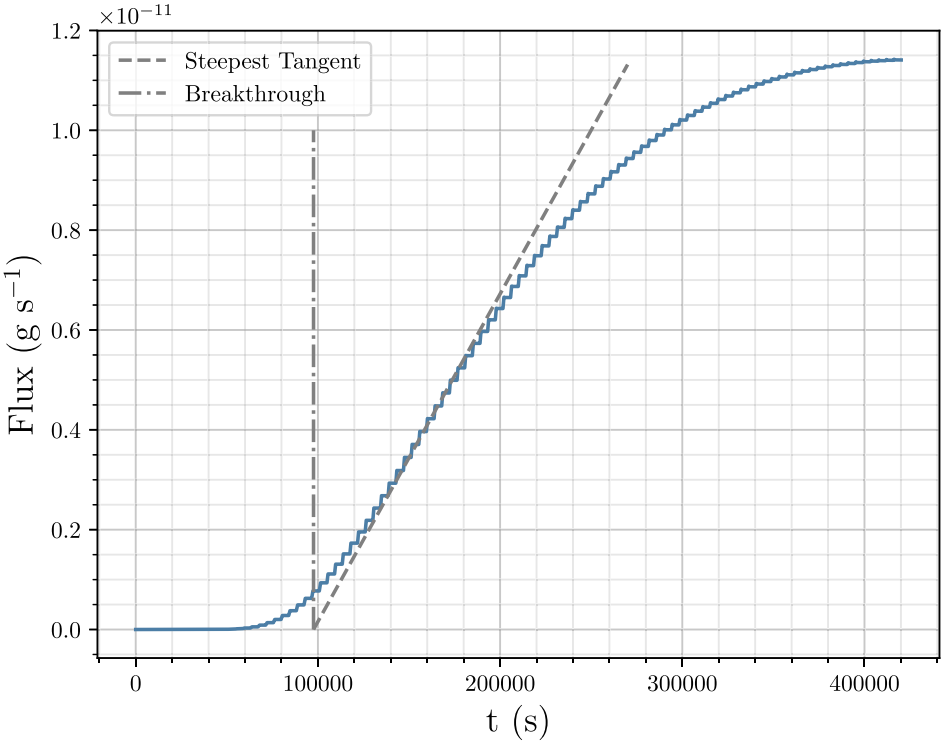

Fig. 11. Temporal evolution of the HIs inventory in the monoblock over 100 cycles.

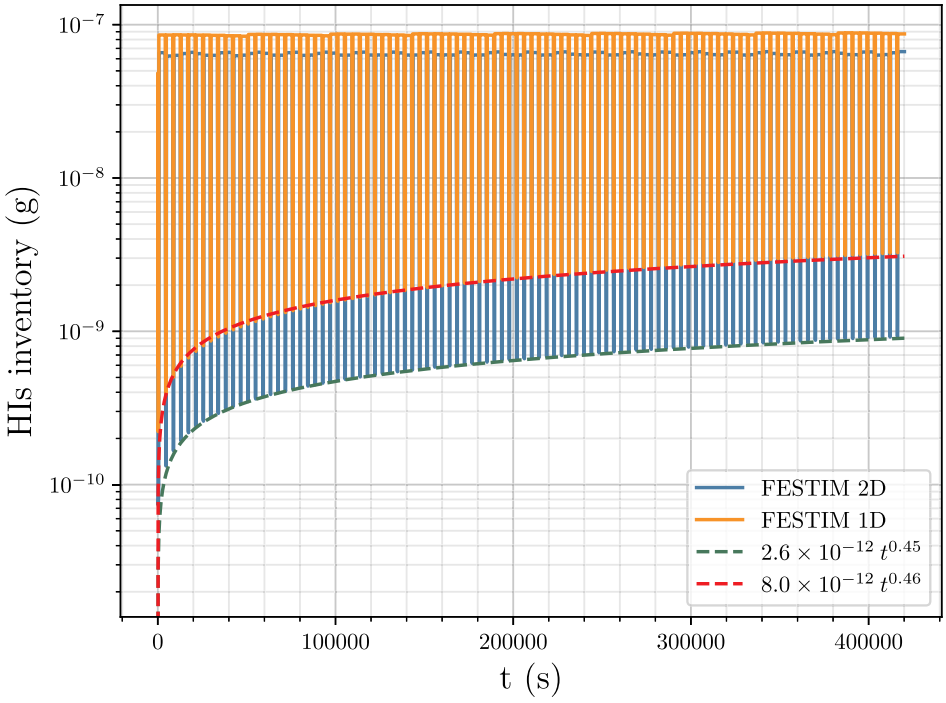

Fig. 12. Temporal evolution of the particle flux through the cooling surface.

$$\text{inv}_{2D} = l \iint (c_{m,2D} + \sum c_{t,i,2D})\, dx\, dy \tag{19}$$

Only 10 cycles are shown on Fig. 13 as Δ_{inv} behaves in a similar way throughout the simulation and varies between − 95% and − 20%. During the resting phases, the error is approximately − 25%. These differences result from the assumption made in the 1D simulation that the simulated retention profile is homogeneous in the monoblock. In this case, it has been shown on Fig. 9 that this assumption was not relevant. It would therefore result in significant errors which could be critical for PFCs design. Moreover, the error during implantation phases keeps increasing with time.

4.2.5. *Influence of interfaces conditions*

In the Section 4.2.4, the influence of the dimension assumptions on the retention results has been investigated. This comparison is based on a very simple assumption for the bi-material interfaces, which is the continuity of the mobile HIs concentration c_m and the related normal flux φ. A more relevant condition, however, relies on the continuity of both the hydrogen chemical potential μ and φ (in a stress-free configuration) [35]:

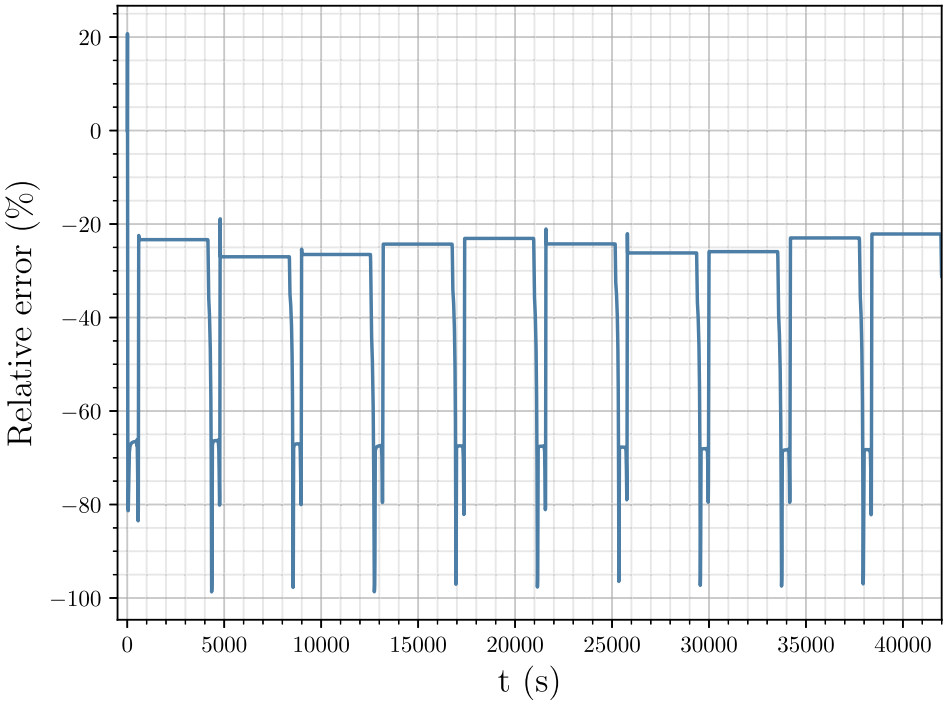

Fig. 13. Temporal evolution of the absolute relative error Δ_{inv}.

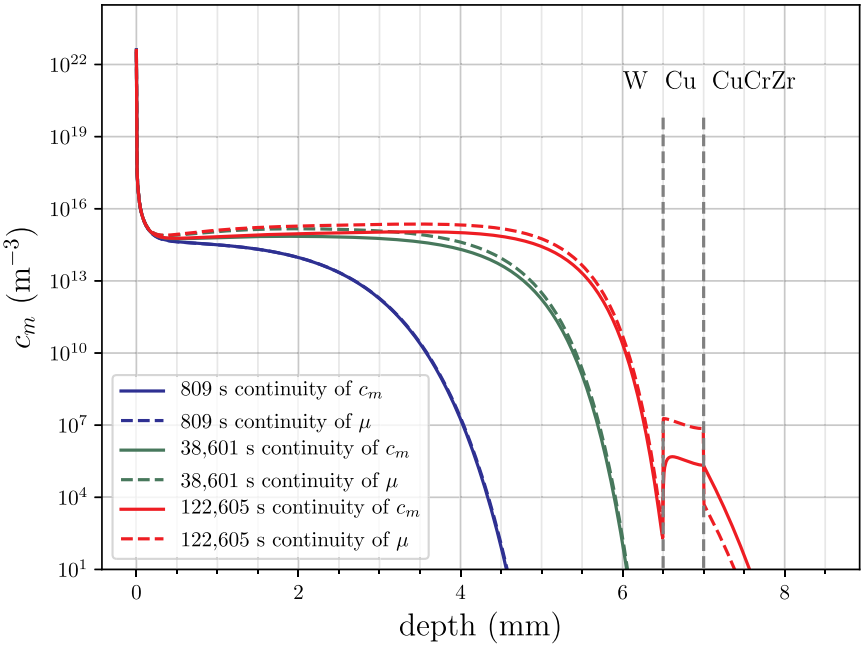

Fig. 14. Influence of the material interfacial conditions on the mobile concentration profile along the AB segment, after several plasma cycles during resting phases.

$$\mu = \mu^0 + RT \ln\left(\frac{c_m}{S}\right) \tag{20}$$

in which μ^0 represents the hydrogen standard chemical potential and S the hydrogen solubility in the considered material. φ is defined as:

$$\varphi = -c_m M \vec{\nabla}\mu \cdot \vec{n} \tag{21}$$

where $M = \frac{D}{RT}$ is the hydrogen mobility and $\vec{n}$ is the normal vector. Such an interfacial condition has been implemented in FESTIM, following the strategy proposed in [36–38] to investigates its influence on the 1D HIs inventory. For the sake of simplicity S is assumed temperature independent in each material. This assumption is valid since this region stays at 400 K throughout the plasma cycles.

The comparison is shown on Figs. 14 and 15, using the following values for the different solubilities at 400 K:

- for W, $1.33 \times 10^{16}\,\mathrm{m^{-3}\cdot Pa^{-0.5}}$ [27]
- for Cu, $1.90 \times 10^{17}\,\mathrm{m^{-3}\cdot Pa^{-0.5}}$ [28]
- for CuCrZr, $3.23 \times 10^{20}\,\mathrm{m^{-3}\cdot Pa^{-0.5}}$ [28]

As expected, on Fig. 14, the concentration profiles are no longer continuous at the interfaces. In tungsten, it appears that the interfacial condition has little influence on the retention profile throughout the simulation time. However, due to solubility differences, c_m notably

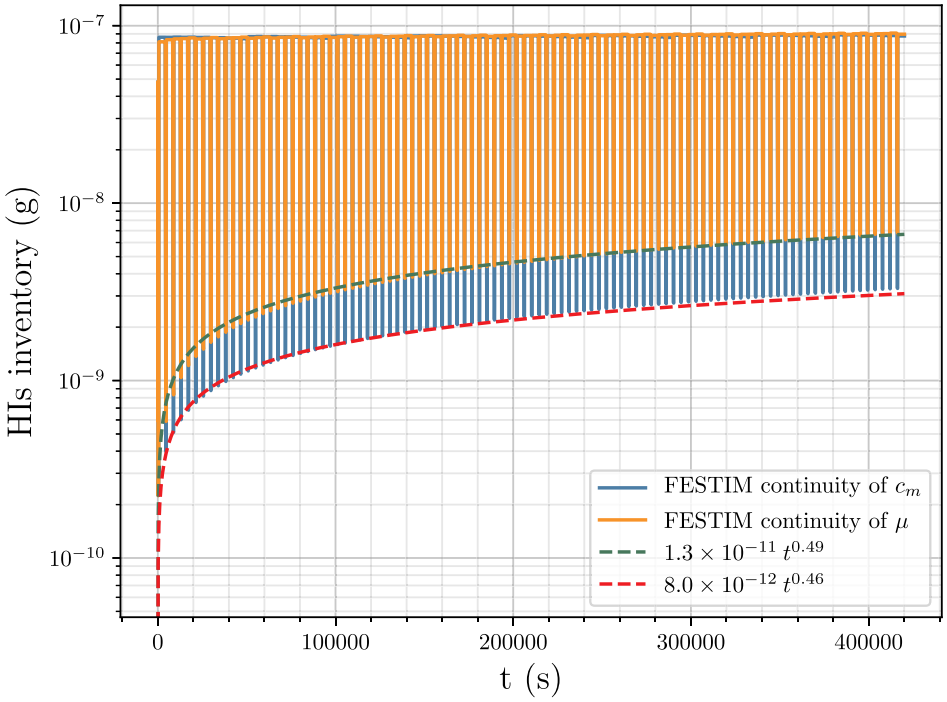

Fig. 15. Influence of the material interfacial conditions on the temporal evolution of the HIs inventory in the monoblock over 100 cycles.

increases in Cu, before decreasing in the CuCrZr layer. These differences induce an increase of the local minima of the HI inventory (Fig. 15), the local maxima being unchanged; the HI inventory evolution exhibits a low sensitivity to the material interface condition.

5. Conclusion

A new code named FESTIM based on MRE model has been developed and includes extrinsic traps creation, transient heat transfer and 2/3D multi-material simulations. Validation and verification have been performed using a well-known TPD experiment from literature, the Method of Manufactured Solutions and a well-known analytical solution. It has been shown that FESTIM can reliably reproduce experimental results and that its governing equations were solved correctly. FESTIM offers the ability to simulate large problems quicker thus opening up the possibility of performing reactor size simulations of HIs migration.

FESTIM has then been used to simulate HIs behaviour in monoblocks during a relevant plasma scenario. At this extent, heat transfers have been simulated at the same time. 2D simulations were needed as edge effects in the resulting fields were significant. In this case, unidimensional approximation could not be made. The error between 1D and 2D simulations was indeed varying between -95% and -20%, thus showing the need of 2D modelling. Results show that for 27,777 monoblocks, the total HIs inventory in the tokamak could reach 1.8 mg after 100 pulses and that it is mostly dominated by retention in the near surface of the monoblocks. Breakthrough time for particle flux at the cooling channel is estimated to be $t = 1 \times 10^5$s which corresponds to 24 cycles. The particle flux stays below 1.2×10^{-11}g·s^{-1}.

One must however be aware that several assumptions have been made. Some properties of Cu and CuCrZr are not yet well known but it is assumed that they have few impact at the macroscopic scale. The plasma scenario encountered in a real tokamak environment could also differ from the one presented here. By extrapolating to the whole tokamak, the assumption is also made that the implantation flux and the heat flux are homogeneous along the whole divertor. Finally, flux and concentration continuity is assumed at the interfaces between the different materials. The effect of interfacial conditions has been investigated and shows low impact on maximum retention. Further work is still required in order to fully investigate these effects. Having a discontinuity induced by an energy barrier would tend to increase retention and decrease or at least delay the flux on the cooling pipe. Further characterisation studies are also required to clearly identify the influence or interfaces on HIs behaviour.

Declaration of Competing Interest

The authors declare that they have no known competing financial interests or personal relationships that could have appeared to influence the work reported in this paper.

Acknowledgements

We would like to express our gratitude to G. De Temmerman from ITER Organization with whom we had many scientific exchanges about the contents of this paper. This work has been carried out within the framework of the EUROfusion Consortium and has received funding from the Euratom Research and Training Programme 2014–2018 and 2019–2020 under grant agreement No 633053. The views and opinions expressed herein do not necessarily reflect those of the European Commission.

References

[1] E.A. Hodille, E. Bernard, S. Markelj, J. Mougenot, C.S. Becquart, R. Bisson, C. Grisolia, Estimation of the tritium retention in ITER tungsten divertor target using macroscopic rate equations simulations, Physica Scripta T170 (2017) 014033, https://doi.org/10.1088/1402-4896/aa8787.
[2] G.D. Temmerman, M. Baldwin, D. Anthoine, K. Heinola, A. Jan, I. Jepu, J. Likonen, C. Lungu, C. Porosnicu, R. Pitts, Efficiency of thermal outgassing for tritium retention measurement and removal in iter, Nucl. Mater. Energy 12 (2017) 267–272, https://doi.org/10.1016/j.nme.2016.10.016.
[3] L. Buzi, G.D. Temmerman, A. Huisman, S. Bardin, T. Morgan, M. Rasinski, R. Pitts, G.V. Oost, Response of tungsten surfaces to helium and hydrogen plasma exposure under ITER relevant steady state and repetitive transient conditions, Nuclear Fusion 57 (12) (2017) 126009, https://doi.org/10.1088/1741-4326/aa81e4.
[4] S. Cui, M. Simmonds, W. Qin, F. Ren, G.R. Tynan, R.P. Doerner, R. Chen, Thermal conductivity reduction of tungsten plasma facing material due to helium plasma irradiation in pisces using the improved 3-omega method, J. Nucl. Mater. 486 (2017) 267–273, https://doi.org/10.1016/j.jnucmat.2017.01.023.
[5] S. Qu, H. Sun, A. Kreter, Y. Yuan, L. Cheng, Z. Huang, B. Xu, W. Chen, W. Cui, Z. Tang, Y. Jia, Y. Lian, X. Liu, W. Liu, Degradation of thermal conductivity of the damaged layer of tungsten irradiated by helium-plasma, Fusion Eng. Des. 137 (2018) 97–103, https://doi.org/10.1016/j.fusengdes.2018.08.014.
[6] M. Wirtz, M. Berger, A. Huber, A. Kreter, J. Linke, G. Pintsuk, M. Rasinski, G. Sergienko, B. Unterberg, Influence of helium induced nanostructures on the thermal shock performance of tungsten, Nucl. Mater. Energy 9 (2016) 177–180, https://doi.org/10.1016/j.nme.2016.07.002.
[7] E. Hodille, X. Bonnin, R. Bisson, T. Angot, C. Becquart, J. Layet, C. Grisolia, Macroscopic rate equation modeling of trapping/detrapping of hydrogen isotopes in tungsten materials, J. Nucl. Mater. 467 (2015), https://doi.org/10.1016/j.jnucmat.2015.06.041.
[8] D. Xie, New solution decomposition and minimization schemes for poissonboltzmann equation in calculation of biomolecular electrostatics, J. Comput. Phys. 275 (2014) 294–309, https://doi.org/10.1016/j.jcp.2014.07.012.
[9] J. Shimwell, R. Delaporte-Mathurin, J.-C. Jaboulay, J. Aubert, C. Richardson, C. Bowman, A. Davis, A. Lahiff, J. Bernardi, S. Yasin, X. Tang, Multiphysics analysis with CAD-based parametric breeding blanket creation for rapid design iteration, Nucl. Fusion 59 (4) (2019) 046019, https://doi.org/10.1088/1741-4326/ab0016.
[10] M.S. Alnæs, J. Blechta, J. Hake, A. Johansson, B. Kehlet, A. Logg, C. Richardson, J. Ring, M.E. Rognes, G.N. Wells, The fenics project version 1.5, Arch. Numer. Softw. 3 (100) (2015), https://doi.org/10.11588/ans.2015.100.20553.
[11] S. Benannoune, Y. Charles, J. Mougenot, M. Gasperini, G. De Temmerman, Numerical simulation by finite element modelling of diffusion and transient hydrogen trapping processes in plasma facing components, Nucl. Mater. Energy 19 (2019) 42–46, https://doi.org/10.1016/j.nme.2019.01.023.
[12] O.V. Ogorodnikova, Trapping Effect In Hydrogen Retention In Metals, Springer Netherlands, Dordrecht, pp. 7–15. 10.1007/978-94-010-0444-2_2.
[13] G. Longhurst, J. Ambrosek, Verification and validation of the tritium transport code tmap7, Fusion Science and Technology 48 (2004).
[14] B. Dudson, J. Madsen, J. Omotani, P. Hill, L. Easy, M. Liten, Verification of bout++ by the method of manufactured solutions, Phys. Plasmas 23 (2016), https://doi.org/10.1063/1.4953429.
[15] P. J. Roache, Code verification by the method of manufactured solutions, J. Fluids Eng. 124 (2002) 4, https://doi.org/10.1115/1.1436090.
[16] O. Ogorodnikova, J. Roth, M. Mayer, Deuterium retention in tungsten in dependence of the surface conditions, J. Nucl. Mater. 313–316 (2003) 469–477, https://doi.org/10.1016/S0022-3115(02)01375-2.
[17] X. Bonnin, E. Hodille, N. Ning, C. Sang, C. Grisolia, Rate equations modeling for hydrogen inventory studies during a real tokamak material thermal cycle, J. Nucl. Mater. 463 (2015) 970–973, https://doi.org/10.1016/j.jnucmat.2014.10.053.
[18] J.F. Ziegler, M. Ziegler, J. Biersack, Srim the stopping and range of ions in matter (2010), Nucl. Instrum. Methods Phys. Res. 268 (11) (2010) 1818–1823, https://doi.org/10.1016/j.nimb.2010.02.091.
[19] L. Sun, S. Jin, H.-B. Zhou, Y. Zhang, W. Zhang, Y. Ueda, H.T. Lee, G.-H. Lu, Critical concentration for hydrogen bubble formation in metals, J. Phys. 26 (39) (2014) 395402, https://doi.org/10.1088/0953-8984/26/39/395402.
[20] N. Fernandez, Y. Ferro, D. Kato, Hydrogen diffusion and vacancies formation in tungsten: density functional theory calculations and statistical models, Acta Materialia 94 (2015) 307–318, https://doi.org/10.1016/j.actamat.2015.04.052.
[21] K. Ohsawa, F. Nakamori, Y. Hatano, M. Yamaguchi, Thermodynamics of hydrogen-induced superabundant vacancy in tungsten, J. Nucl. Mater. 458 (2015) 187–197, https://doi.org/10.1016/j.jnucmat.2014.12.029.
[22] D. Kato, H. Iwakiri, Y. Watanabe, K. Morishita, T. Muroga, Super-saturated hydrogen effects on radiation damages in tungsten under the high-flux divertor plasma irradiation, Nucl. Fusion 55 (8) (2015) 083019, https://doi.org/10.1088/0029-5515/55/8/083019.
[23] E.A. Hodille, N. Fernandez, Z.A. Piazza, M. Ajmalghan, Y. Ferro, Hydrogen supersaturated layers in h/d plasma-loaded tungsten: a global model based on thermodynamics, kinetics and density functional theory data, Phys. Rev. Mater. 2 (2018) 093802, https://doi.org/10.1103/PhysRevMaterials.2.093802.
[24] J. Condon, T. Schober, Hydrogen bubbles in metals, J. Nucl. Mater. 207 (1993) 1–24, https://doi.org/10.1016/0022-3115(93)90244-S.
[25] M. Poon, R. Macaulay-Newcombe, J. Davis, A. Haasz, Flux dependence of deuterium retention in single crystal tungsten, J. Nucl. Mater. 307–311 (2002) 723–728, https://doi.org/10.1016/S0022-3115(02)00946-7.
[26] V. Alimov, J. Roth, M. Mayer, Depth distribution of deuterium in single- and polycrystalline tungsten up to depths of several micrometers, J. Nucl. Mater. 337 (2005) 619–623, https://doi.org/10.1016/j.jnucmat.2004.10.082.
[27] R. Frauenfelder, Solution and diffusion of hydrogen in tungsten, J. Vacuum Sci. Technol. 6 (1969) 388–397, https://doi.org/10.1116/1.1492699.
[28] I. Pealva, G. Alberro, F. Legarda, G.A. Esteban, B. Riccardi, Interaction of copper

alloys with hydrogen, in: L. Collini (Ed.), Copper Alloys, IntechOpen, Rijeka, 2012, , https://doi.org/10.5772/34469.
[29] R.A. Anderl, D.F. Holland, G.R. Longhurst, R.J. Pawelko, C.L. Trybus, C.H. Sellers, Deuterium transport and trapping in polycrystalline tungsten, Fusion Technol. 21 (2P2) (1992) 745–752, https://doi.org/10.13182/FST92-A29837.
[30] K. Tsukatani, Y. Ueda, K. Tanimoto, H.T. Lee, Y. Ohtsuka, M. Taniguchi, T. Inoue, K. Sakamoto, I. Takagi, N. Yoshida, Deuterium retention in damaged tungsten, Fusion Sci. Technol. 60 (4) (2011) 1543–1547, https://doi.org/10.13182/FST11-A12727.
[31] J. Yu, M. Simmonds, M. Baldwin, R. Doerner, Deuterium retention in re-solidified tungsten and beryllium, Nuclear Mater. Energy 18 (2019) 297–306, https://doi.org/10.1016/j.nme.2019.01.011.
[32] A. Durif, M. Richou, G. Kermouche, M. Lenci, J.-M. Bergheau, Impact of tungsten recrystallization on iter-like components for lifetime estimation, Fusion Eng. Design 138 (2019) 247–253, https://doi.org/10.1016/j.fusengdes.2018.11.003.
[33] R. Anderl, M. Hankins, G. Longhurst, R. Pawelko, Deuterium transport in Cu, CuCrZr, and Cu/Be, J. Nucl. Mater. 266–269 (1999) 761–765, https://doi.org/10.1016/S0022-3115(98)00878-2.
[34] E. Hodille, Study and modeling of the deuterium trapping in ITER relevant materials, Univeristá d'Aix-Marseille, 2016 Phd.
[35] Y. Gu, J.A. El-Awady, Quantifying the effect of hydrogen on dislocation dynamics: a three-dimensional discrete dislocation dynamics framework, J. Mech. Phys. Solids 112 (2018) 491–507, https://doi.org/10.1016/j.jmps.2018.01.006.
[36] S. Yoon, B. Han, Z. Wang, On moisture diffusion modeling using thermal-Moisture analogy, J. Electron. Packaging 129 (4) (2007) 421–426, https://doi.org/10.1115/1.2804090.
[37] C. Jang, S. Park, B. Han, S. Yoon, Advanced thermal-Moisture analogy scheme for anisothermal moisture diffusion problem, J. Electron. Packaging 130 (1) (2008), https://doi.org/10.1115/1.2837521.
[38] D. Liu, J. Wang, R. Liu, S.B. Park, An examination on the direct concentration approach to simulating moisture diffusion in a multi-material system, Microelectron. Reliab. 60 (2016) 109–115.